Earth and Planetary Science Letters 618 (2023) 118296

Contents lists available at ScienceDirect

Earth and Planetary Science Letters

journal homepage: www.elsevier.com/locate/epsl

Compressibility of ferropericlase at high-temperature: Evidence for the iron spin crossover in seismic tomography

Viktoria E. Trautner [a,*], Stephen Stackhouse [b], Alice R. Turner [a], Paula Koelemeijer [a,c], D. Rhodri Davies [d], Alba San José Méndez [e], Niccolo Satta [a], Alexander Kurnosov [f], Hanns-Peter Liermann [e], Hauke Marquardt [a]

[a] Department of Earth Sciences, University of Oxford, OX1 3AN Oxford, United Kingdom
[b] School of Earth and Environment, University of Leeds, LS2 9JT Leeds, United Kingdom
[c] Department of Earth Sciences, Royal Holloway University of London, TW20 0EX Egham, United Kingdom
[d] The Research School of Earth Sciences, Australian National University, ACT 2600 Canberra, Australia
[e] Deutsches Elektronen-Synchrotron (DESY), 22607 Hamburg, Germany
[f] Bayerisches Geoinstitut BGI, University of Bayreuth, 95440 Bayreuth, Germany

ARTICLE INFO

Article history:
Received 14 March 2023
Received in revised form 22 June 2023
Accepted 27 June 2023
Available online 13 July 2023
Editor: J. Badro

Keywords:
ferropericlase
lower mantle
spin crossover
elastic softening
ab initio computations
seismic tomography

ABSTRACT

The iron spin crossover in ferropericlase, the second most abundant mineral in Earth's lower mantle, causes changes in a range of physical properties, including seismic wave velocities. Understanding the effect of temperature on the spin crossover is essential to detect its signature in seismic observations and constrain its occurrence in the mantle. Here, we report the first experimental results on the spin crossover-induced bulk modulus softening at high temperatures, derived directly from time-resolved x-ray diffraction measurements during continuous compression of $(Mg_{0.8}Fe_{0.2})O$ in a resistive-heated dynamic diamond-anvil cell. We present new theoretical calculations of the spin crossover at mantle temperatures benchmarked by the experiments. Based on our results, we create synthetic seismic tomography models to investigate the signature of the spin crossover in global seismic tomography. A tomographic filter is applied to allow for meaningful comparisons between the synthetic models and data-based seismic tomography models, like SP12RTS. A negative anomaly in the correlation between V_s variations and V_c variations (S-C correlation) is found to be the most suitable measure to detect the presence of the spin crossover in tomographic models. When including the effects of the spin crossover, the misfit between the synthetic model and SP12RTS is reduced by 63%, providing strong evidence for the presence of the spin crossover, and hence ferropericlase, in the lower mantle. Future improvement of seismic resolution may facilitate a detailed mapping of spin state using the S-C correlation, providing constraints on mantle temperatures by taking advantage of the temperature sensitivity of the spin crossover.

1. Introduction

$(Mg_{1-x}Fe_x)O$ ferropericlase is the second most abundant mineral in a pyrolitic lower mantle, constituting approximately 18% by volume (Irifune et al., 2010). Under pressures relevant to the lower mantle, the iron atoms in ferropericlase gradually undergo a spin-pairing transition from high-spin (HS) to low-spin (LS) state, where d-electrons are redistributed over atomic orbitals (Badro et al., 2003). As a result, the ionic radius of iron is reduced and the unit-cell volume of ferropericlase decreases, causing an anomalous softening of the bulk modulus across the spin crossover (Crowhurst et al., 2008; Fei et al., 2007b; Lin et al., 2005; Marquardt et al., 2009, 2018; Solomatova et al., 2016; Wentzcovitch et al., 2009; Wu et al., 2013; Yang et al., 2015; Méndez et al., 2022). The spin crossover-induced bulk modulus softening has been reported to cause major changes in a wide range of properties of ferropericlase that are relevant for large-scale geophysical processes (Lin et al., 2013). Therefore, detecting the signature of the spin crossover in seismic observations and constraining its occurrence and distribution in the lower mantle is of vital importance to improve geodynamic models and constrain chemical heterogeneity in the mantle. In an ideal case, it would be possible to construct three-dimensional (3D) maps of lateral and vertical variations in the spin state of ferropericlase based on seismic tomography.

* Corresponding author.
E-mail address: viktoria.trautner@earth.ox.ac.uk (V.E. Trautner).

https://doi.org/10.1016/j.epsl.2023.118296

The enhanced compressibility of ferropericlase in the mixed-spin (MS) region causes a drop in P-wave (V_P) and bulk sound velocities (V_C), while no substantial effect of the spin crossover on the shear modulus (G) and S-wave velocities (V_S) has been reported (Marquardt et al., 2009; Murakami et al., 2012; Wu et al., 2013; Yang et al., 2015). Consequently, a high ratio of V_S to V_P and negative correlation between V_S and V_C are seen as characteristic features of the spin crossover, that might allow for its detection in seismic observations (Marquardt et al., 2009). However, the depth, broadness and shape of the iron spin crossover are not yet well-constrained at temperatures of the lower mantle, hampering a robust detection by seismic methods. Previous experimental studies at high temperature did not measure the bulk modulus of ferropericlase directly, but had to rely on assumptions about its behaviour across the spin crossover (Mao et al., 2011) or have been limited to low iron contents and pressures below the onset of the spin crossover (Yang et al., 2016). While theoretical calculations generally predict that the spin crossover broadens and shifts to higher pressures with increasing temperature (Holmström and Stixrude, 2015; Sun et al., 2022; Tsuchiya et al., 2006; Wentzcovitch et al., 2009; Wu et al., 2013), a verification of different computational predictions has been hampered by the absence of an experimental benchmark. Calculated spin state phase diagrams show major differences depending on the assumptions made, leading to significant uncertainties in any attempt to detect the spin crossover signature in seismic observables (e.g. Sun et al., 2022).

Nevertheless, first efforts to identify the spin crossover signal in seismological models have been reported (Cammarano et al., 2010; Kennett, 2021; Shephard et al., 2021). In particular, recent work by Shephard et al. (2021) takes advantage of the differing effects of the spin crossover on P- and S-wave velocities, suggesting that the spin crossover might be detectable in cold parts of the lower mantle. However, in addition to the current mineral physics uncertainties, the seismic tomography models investigated in the previous work lack internal consistency and realistic seismic resolution has not been accounted for.

Here, we present the first direct experimental determination of the bulk modulus softening of ferropericlase across the spin crossover at high temperature. We further present a new theoretical model that reproduces our high-temperature experimental results, as well as previous measurements at room temperature, allowing us to robustly predict the signature of the spin crossover at relevant mantle temperatures. We use these experimentally-verified computations to convert the 3D temperature variations predicted by a geodynamic model to high-resolution maps of seismic velocity variations in the lower mantle. By applying a tomographic filter, we are able to directly compare the results from our synthetic tomography model to tomographic model SP12RTS (Koelemeijer et al., 2016), a joint P- and S-wave model. We demonstrate that the fit between the synthetic model and SP12RTS is improved when the effects of the spin crossover in ferropericlase are included. Our study thus provides strong indications that the spin crossover in ferropericlase occurs in the Earth's mantle and that lateral and vertical variations in spin state may be investigated using seismic tomography models.

2. Methods

2.1. Experimental approach

Powder of $(Mg_{0.8}Fe_{0.2})O$ was synthesized from stoichiometric mixtures of reagent grade MgO and Fe_2O_3, treated in a gas-mixing furnace at 1250 °C at an oxygen fugacity 2 log units below the fayalite-magnetite-quartz (FMQ) buffer (Marquardt and Miyagi, 2015). Platinum powder was mixed with the sample as pressure marker and this mixture was loaded in two diamond-anvil cells (DACs), RH1 and RH2, with 150 μm culet size diamonds. Rhenium gaskets with inserts of $Fe_{0.79}Si_{0.06}B_{0.15}$ metallic glass were used to avoid parasitic Re peaks (Dong et al., 2022). No pressure-transmitting medium (PTM) was used, due to experimental difficulties in using a gas PTM at the high temperatures of our experiments and the fact that additional strong XRD reflections from a solid medium would complicate analysis of the data. A resistive-heated dynamic DAC (rh-dDAC) setup, that was developed at beamline P02.2 at PETRAIII, DESY, Germany (Méndez et al., 2020) was employed to continuously compress ferropericlase across the spin crossover pressure range. During compression, time-resolved X-ray diffraction measurements were conducted, which allowed us to collect quasi-continuous volume-pressure data. The compression experiments were performed at P02.2 using monochromatic synchrotron x-ray radiation with a fixed wavelength of 0.4836 Å. A fast GaAs 2.3 LAMBDA detector (Pennicard et al., 2018) was employed to collect diffraction images with single image exposure times of 200 ms, capturing about 20% of the Debye-Scherrer diffraction rings.

Two types of experiments were conducted in the rh-dDAC (see Supporting Information SI fig. S1): (1) Continuous compression along a pre-programmed pressure ramp (e.g. Méndez et al., 2020), and (2) pressure cycling over a limited pressure interval (Marquardt et al., 2018). In cell RH1, a total of three ramp experiments were measured at ~900 K. Single diffraction images were collected every ~50 K during heating to target temperature and the sample was cooled down to room temperature between ramps. During heating before the third ramp, 3.5 sinusoidal pressure oscillations of 0.2 Hz were applied to the sample every ~50 K. The amplitude of the cycling is related to the voltage applied to the piezo-actuator and the tightness of the cell and varied from 1-3 GPa (SI table S1). A single compression ramp was measured at ~1100 K in cell RH2. The cell was then cooled down to room temperature and heated again to 1450 K, while pressure cycling measurements with amplitudes of 1-19 GPa were conducted every ~50 K. Maximum compression rates during ramp experiments ranged from 0.17 GPa/s to 0.3 GPa/s and pressure increased by 16-34 GPa in each ramp, together covering pressures between 33 GPa and 105 GPa (SI table S1). We note that static compression data at room temperature from Lin et al. (2005) and previous dDAC measurements from Méndez et al. (2022) with compression rates up to 1.2 GPa/s (Fig. 1) are in excellent agreement, i.e. our results are expected to be generally comparable to those derived during resistive-heating under static compression, but with largely increased pressure-resolution. Temperature measurements before and after each run from two type-R thermocouples mounted close to the tips of the diamonds were used to estimate temperature variations during the experimental run, which were less than 3%.

The program Dioptas (Prescher and Prakapenka, 2015) was used to integrate and background-correct diffraction images. A Python code for batch-processing of time-resolved diffraction data (Wang, 2022) was used on the integrated data to extract the peak positions of ferropericlase and platinum. The average unit-cell volume of platinum from the $(111)_{Pt}$, $(200)_{Pt}$ and $(220)_{Pt}$ reflections, weighted by the uncertainty of the peak-fit, was used to derive pressure, employing previously published third-order Birch-Murnaghan equation of state (EoS) parameters (Fei et al., 2007a). Similarly, the unit-cell volume of ferropericlase was derived from the weighted average of the $(111)_{Fp}$, $(200)_{Fp}$ and $(220)_{Fp}$ reflections. Line-shift analysis of the utilized reflections (Singh and Takemura, 2001) showed that the differential stresses present during the ramp experiment measured in cell RH2 at 1100 K were high compared to the other experiments (SI section S1.1 and fig. S2). We found that the volumes derived from the $(111)_{Fp}$ and $(220)_{Fp}$ reflections are closest to the volumes measured during the pressure oscillation experiments at the same temperature and under lower

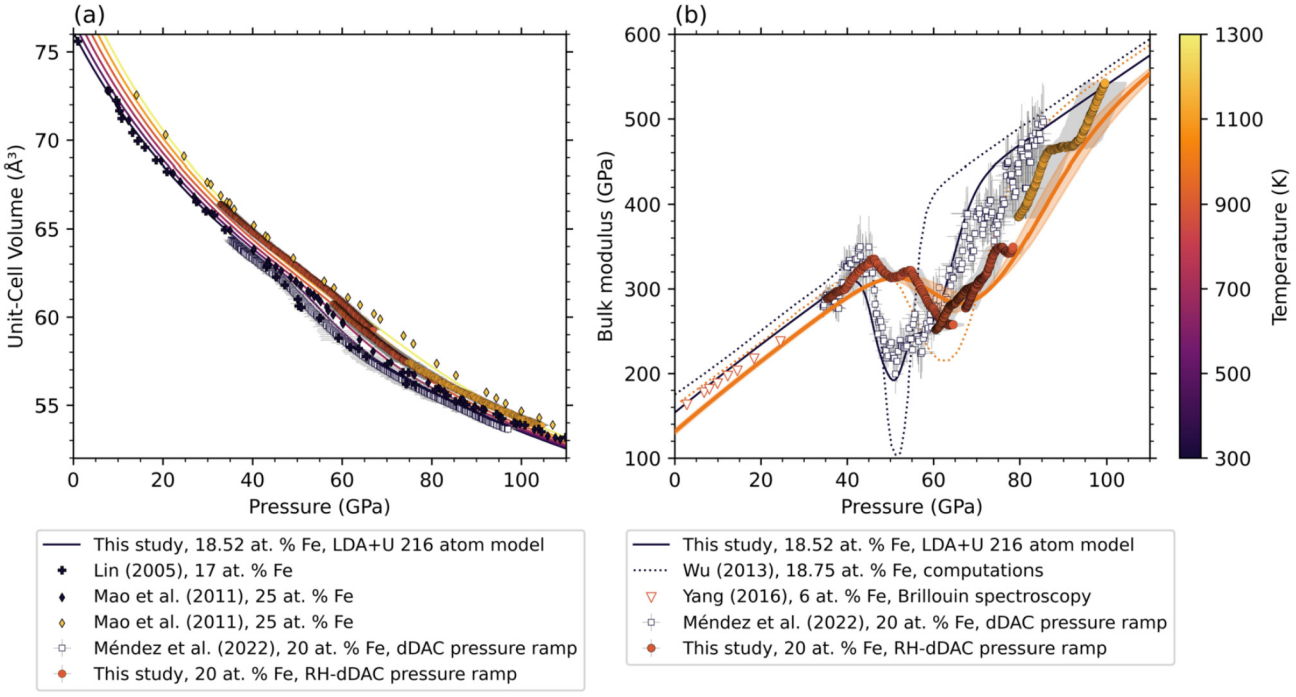

Fig. 1. (a) Volume-pressure (V-P) data collected during pressure ramp experiments in the RH-dDAC at 900-1100 K (filled circles), together with the predicted V-P curves along isotherms from our numerical calculations. Also shown are previous results of a pressure ramp experiment at room temperature (open squares, Méndez et al., 2022), as well as results from Lin et al. (2005) (static compression at room temperature, filled crosses) and from Mao et al. (2011) (static compression at room temperature and at 1200 K with laser heating, filled diamonds). (b) Experimental bulk moduli as a function of pressure at high temperature, derived from pressure ramp experiments (filled circles). The grey shaded region indicates the pressure interval over which the V-P curve was differentiated to derive the bulk modulus. The 1000 ± 100 K isotherm from our lattice dynamics calculations is shown as a solid orange line with a shaded region and the 300 K isotherm is indicated by a solid dark line. Previous results from dDAC ramp experiments at room temperature are shown as open squares (Méndez et al., 2022). Also shown are Brillouin spectroscopy results at 900 K (open triangles, Yang et al., 2016), as well as previous computational results at 300 K and 1000 K (dotted lines, Wu et al., 2013). Note that the results from both Yang et al. (2016) and Wu et al. (2013) are for the adiabatic bulk modulus, whereas the results from this study and Méndez et al. (2022) are for the isothermal bulk modulus.

stress conditions. Therefore, we chose to use the weighted average of the volumes from the $(111)_{Fp}$ and $(220)_{Fp}$ reflections only for the ramp at 1100 K. Uncertainties in pressure and unit-cell volume of ferropericlase were estimated from the difference between diffraction lines.

The smooth nature and high pressure-resolution of the compression ramps permits direct calculation of the isothermal bulk modulus (K_T) by numerical differentiation, according to its thermodynamic definition: $K_T = -V \cdot \frac{\partial P}{\partial V}\big)_T$ (Méndez et al., 2021). K_T is calculated from the slope of a linear fit to measured volumes V as a function of pressure, i.e. $V(P)$, that fall in a chosen pressure interval around the target pressure. The error in K_T is propagated from the uncertainty in V and the standard error of the slope of the linear fit. When choosing the pressure interval, there is a trade-off between the uncertainties in the derived bulk moduli and the effective pressure resolution (Méndez et al., 2022). An interval of 5 GPa was found to be the best compromise for the ramps measured in RH1, while a 10 GPa interval was used for the ramp measured in RH2. Following Marquardt et al. (2018), the $V(P)$ data collected during pressure cycling at seismic frequencies was also used to calculate the bulk modulus at each temperature step (SI section 1.2). The quality of the diffraction images collected during pressure cycling in RH2 was not sufficient to extract a reliable bulk modulus value from the $V(P)$ data.

2.2. Ab-initio calculations

Two types of calculations were performed. Lattice dynamics calculations were performed to determine the difference in the static and vibrational free energy of ferropericlase in different spin states, allowing calculation of the spin crossover. Molecular dynamics simulations were performed to determine the elastic properties of ferropericlase in a fixed high or low-spin state. Both sets of results were combined to estimate the properties of ferropericlase through the spin crossover. For all calculations we used the Vienna Ab-initio Simulation Package (VASP) (Kresse and Furthmüller, 1996a,b) employing the projector augmented wave method (Blöchl, 1994; Kresse and Joubert, 1999), within the framework of density functional theory (DFT). The local density approximation (LDA) (Perdew and Zunger, 1981) was used for the exchange-correlation functional. The valence electron configurations for the potentials were $2p^6 3s^2$ for Mg, $3p^6 3d^7 4s^1$ for Fe, and $2s^2 2p^4$ for O. The cut-off for the plane-wave basis set was set to 600 eV.

In order to describe the correlated d electrons of iron in ferropericlase, we utilized the LDA+U scheme of Dudarev et al. (1998), in which only the difference between onsite Coulomb interaction parameter U and onsite exchange parameter J is meaningful. In the present work, we used U - J = 3.3 eV, which was found to lead to the best agreement with experimental values for the spin crossover pressure in ferropericlase at 300 K (Méndez et al., 2022), and is similar to the 3.0 eV used in other studies of the spin crossover (Muir and Brodholt, 2015). Since the LDA is known to underestimate pressure, we calculated a correction using the method outlined by Oganov et al. (2001), including the thermal pressure term calculated from our lattice dynamics calculations. The correction was calculated to be +3.5 GPa, based on the ambient condition volume of 76.1 Å^3 reported by (Lin et al., 2005). This correction is applied to our high-temperature results (both lattice dynamics and molecular dynamics) before their use in the synthetic tomography models.

2.2.1. Approach to spin transition calculations

In their pioneering work, Tsuchiya et al. (2006) and Wentzcovitch et al. (2009) calculated the fraction of LS iron in ferropericlase from an expression similar to:

$$n(P,T) = \frac{1}{1 + m(2S+1)\left(\frac{\Delta G_{HS-LS}(P,T)}{k_B X_{Fe} T}\right)}, \quad (1)$$

where m is the electronic configuration degeneracy ($m = 3$ for HS and $m = 1$ for LS), S is the spin quantum number ($S = 2$ for HS and $S = 0$ for LS), $\Delta G_{HS-LS}(P,T)$ is the difference between the static and vibrational components of the Gibbs free energy of the high- and low-spin states, X_{Fe} is the fraction of iron, and k_B is the Boltzmann constant. This derivation assumes ideal mixing of high- and low-spin ions. We will refer to this approach as the single spin transition method (SSTM), since it only involves calculation of $\Delta G_{HS-LS}(P,T)$ for a single transition (from full HS to full LS). This method tends to lead to a spin crossover that is narrower at ambient temperature than experimental results (Méndez et al., 2022).

Later work by Holmström and Stixrude (2015) demonstrated that favourable enthalpy of mixing of high- and low-spin ions leads to a broader spin crossover. Further studies have proposed alternative methods, which include a non-ideal mixing model, with and without the contribution of magnetic entropy (Sun et al., 2022). Building on this, we recently showed that good agreement is obtained with ambient temperature experimental results if, rather than assuming ideal mixing of high- and low-spin states, one calculates the series of successive spin transitions between stable spin states, from high- to low-spin (Méndez et al., 2022). In this method, Equation (1) is applied to each individual spin transition, where $\Delta G_{HS-LS}(P,T)$ is now the difference between the static and vibrational components of the Gibbs free energy of the higher and lower spin states and X_{Fe} is the fraction of iron weighted by the fraction of iron involved in the spin transition. The overall n value for a model is then a weighted average of the n values for the individual spin transitions, where the weights are the fraction of iron atoms in the model involved in the successive spin transitions. We will refer to this approach as the multiple spin transition method (MSTM), as it requires the calculation of $\Delta G_{HS-LS}(P,T)$ for multiple spin transitions.

Preliminary calculations showed that differences in the results of the SSTM and MSTM are only significant at low temperature (<1000 K), where it is possible for a spin transition in one particular iron atom to finish before it begins in another. Experimental results at 300 K (Méndez et al., 2022) are reproduced best by the MSTM (SI fig. S5). At lower mantle temperatures (ranging from approximately 1800 K at the top to 4000 K at the core-mantle boundary), both methods lead to similar results (SI figs. S6-S7), since all iron atoms are undergoing a spin transition and so the order of the spin transitions is irrelevant. Here, we chose to use the MSTM to compare with experimental results between 300 K and 1450 K, since the MSTM is expected to reproduce results below 1000 K better than the SSTM.

2.2.2. Spin state calculations

Prior to performing lattice dynamics calculations, we investigated the effect of model size and arrangement of iron atoms on the spin crossover (SI sections S2-S3 and figs. S3-S6). Based on the results, we selected a 216-atom ferropericlase model (Configuration 10) with a $(Mg_{0.8148}Fe_{0.1852})O$ composition (i.e. 20 iron atoms in the model) for our production calculations. This model is larger than those in our previous work (Méndez et al., 2022), allowing on-axis iron atom neighbour pairs, while avoiding infinite repeating sequences of Fe and O atoms, arising from finite-size effects associated with the use of periodic boundary conditions. The latter was shown to have a non-negligible effect on the calculated spin crossover (Méndez et al., 2022). In accordance with the observations of Waychunas et al. (1994), the positions of the iron atoms were chosen at random. The coordinates of the iron atoms in all models studied in this work are listed in SI tables S2 and S3.

Since it was not feasible to calculate the vibrational free energy for all possible spin states for a 216-atom model, we first calculated the stable mixed-spin states between the high- and low-spin states at 0 K, neglecting the vibrational free energy contribution, and used those to compute the fraction of LS iron (SI sections S3-S5). Lattice dynamics calculations were then performed to calculate the vibrational free energy for only the stable mixed-spin states at 0 K (SI table S4).

For comparison, a small number of spin transition calculations were also performed using a hybrid functional, comprising the LDA with a 0.25 fraction of exact exchange. These results showed good agreement with our LDA+U calculations at 300 K, with some small differences along a mantle geotherm below 1500 km (SI section S5 and fig. S8).

2.2.3. Elastic constants of ferropericlase

Molecular dynamics simulations were used to calculate the elastic properties, as opposed to lattice dynamics calculations, for two reasons: molecular dynamics simulations account for all anharmonic effects, which may become important at lower mantle temperatures; and the large cell used in the lattice dynamics calculations made calculating elastic constants using lattice dynamics prohibitively computationally expensive.

Preliminary calculations showed that the elastic properties of ferropericlase are less sensitive to magnetic state and arrangement of iron than the spin crossover, permitting the use of a smaller 64-atom model for molecular dynamics simulations (SI section S6). The model used has a $(Mg_{0.8125}Fe_{0.1875})O$ composition (i.e. 6 iron atoms in the model) and an arrangement of iron atoms identical to the symmetric model used in our previous work (Méndez et al., 2022). High-temperature elastic constants were calculated for ferropericlase, fixed in a HS and LS state, from molecular dynamics simulations (NVT ensemble) using the Nosé thermostat to maintain constant temperature (Nosé, 1984), see SI section S7 for details. Isothermal and adiabatic elastic properties were calculated at 4 pressures and 6 temperatures. These are shown in SI figure S9 and listed in tables S5 and S6. Comparison of isothermal bulk moduli from our lattice dynamics calculations with those from our molecular dynamics simulations show good agreement (SI section S8 and fig. S10).

To predict elastic constants at other pressures and temperatures a weighted linear least-squares fit was made to values at the same temperature to determine values at the desired temperature and then values at the two nearest pressures points were used to interpolate or extrapolate to the desired pressure (SI fig. S11). To predict densities at other pressures and temperatures a weighted linear least-squares fit was made to values at the same temperature, to determine four values at the desired temperature, and these were then fit using a second-order Birch-Murnaghan equation of state (Birch, 1947; Murnaghan, 1944). To calculate the elastic constants of ferropericlase through the spin crossover we used the equations derived by Wu et al. (2013) (SI section S9).

2.3. Synthetic tomography models

To understand the effect of the iron spin crossover in ferropericlase on global seismic tomography, specifically its effect on the relationships between seismic velocities, we constructed synthetic seismic tomography models from which we can calculate the ratio between V_S and V_P variations (hereafter denoted as S/P ratio)

and the correlation between V_S and V_C variations (here-after denoted as S-C correlation). We follow the methodology employed by Koelemeijer et al. (2018) with some adaptations as described below.

Rather than assuming a random distribution of temperatures in the mantle, we use the predicted present-day temperature distribution in the mantle based on a high-resolution isochemical mantle circulation model (Davies et al., 2012; see Koelemeijer et al., 2018 for more details). To convert these temperature variations to seismic velocities, we employ a thermodynamic database that describes the elastic parameters for any combination of pressure and temperature in the mantle for a given bulk mantle composition. However, existing databases based on thermodynamic mineralogical models (e.g. Stixrude and Lithgow-Bertelloni, 2011, 2022) include ferropericlase only in the HS state.

To obtain the required thermodynamic database for ferropericlase in different spin states, we first linearly interpolate our experimentally-verified computations for density and bulk modulus obtained at a few fixed temperatures (300, 1000, 2000, 3000 and 4000 K) to a spacing of 50 K, before linearly interpolating to every 1 GPa in pressure. We then calculate Voigt-Reuss-Hill average properties for a mantle of pyrolitic composition in a simplified six-component system using the thermodynamic database of Stixrude and Lithgow-Bertelloni (2011, personal communication 2019), but replacing the phase properties of ferropericlase with our results for the MS phase with P-T dependent spin fractions. Note that by calculating a phase weighted average, we implicitly assume that ferropericlase is homogeneously distributed in the mantle. The phase properties for HS ferropericlase in the published model of Stixrude and Lithgow-Bertelloni (2011) match with our new computational results for HS ferropericlase with relative differences of less than 0.5% along the geotherm (SI fig. S12).

We convert the temperatures in the mantle circulation model to seismic velocities using the adapted thermodynamic database, including either our own HS or MS ferropericlase results. The resulting high-resolution seismic mantle models describe realistic mantle structures, that we can use to calculate the relationships between seismic velocities in order to investigate the expected effect of the spin crossover in ferropericlase in the Earth's mantle. Specifically, we calculate the S-C correlation, as well as the S/P ratio. In both cases, we directly use the spherical harmonic coefficients that describe the tomography models after reparameterization, using the same approach as in Koelemeijer et al. (2018). We focus on the radially averaged values of these quantities, in order to remove any geographic dependence due to the plate reconstruction model used in the geodynamic simulation.

We cannot directly compare the high-resolution synthetic models to data-derived tomography models from the literature, because these represent a filtered and weaker version of actual mantle structures. To enable a meaningful comparison, we multiply our high-resolution synthetic models with the resolution matrix of model SP12RTS (Koelemeijer et al., 2016). SP12RTS is one of few existing tomography models that inverted jointly for V_S and V_P variations in the mantle without imposing an a priori scaling, which is crucial for studying the relationships between different seismic velocities. It also provides the associated resolution matrix (or tomographic filtering), which allows us to capture the heterogeneous data coverage and inherent damping of the tomographic inversion. Therefore, we can perform like-to-like and quantitative comparisons between our synthetic tomography models with HS or MS ferropericlase and SP12RTS itself. By calculating the relationships between seismic velocities in both the high-resolution seismic models and the filtered models, we can determine the theoretically expected effect of the spin crossover in the Earth's mantle as well as what we may observe realistically at present in an existing tomography model.

3. Results and discussion

3.1. Comparison of experimental and computational results on the anomalous compressibility of ferropericlase at high temperature

The experimental unit-cell volumes of $(Mg_{0.8}Fe_{0.2})O$ collected in the ramp experiments at 900 K and 1100 K are shown in Fig. 1a as a function of pressure, together with the isotherms from our ab-initio calculations. Previous data collected at 300 K (Lin et al., 2005; Méndez et al., 2022) and at 1200 K in a laser-heated DAC (Mao et al., 2011) are also shown. At approximately 60 GPa, there is a clear drop in the volumes determined from the compression ramps measured at 900 K, which is shifted to higher pressures by about 10 GPa compared to the volumes at 300 K (Méndez et al., 2022). This change in the trend of the $V(P)$ curve is attributed to the onset of the spin crossover. Our experimental data agree well with the new theoretical predictions at most pressures and temperatures. The only previously published data on ferropericlase at high temperature (Komabayashi et al., 2010; Mao et al., 2011) were collected in laser-heated DACs and diverge from our experimental and computational results at pressures above ~40 GPa, where they are shifted to higher pressures and/or volumes (Fig. 1a and SI fig. S13). This may be due to the use of a different pressure standard, an inhomogeneous temperature distribution or chemical segregation that might occur during laser-heating (Sinmyo and Hirose, 2010). We note that there is generally significant disagreement on the onset pressure and width of the spin crossover in existing literature, using a wide range of experimental designs and analytical methods (see for example table 8 in Solomatova et al. (2016)). Some of these differences might arise from limited pressure resolution. The quasi-continuous nature of our compression curves allows us to constrain the spin crossover pressure range more precisely.

We derived the isothermal bulk modulus directly from the slope of our $V(P)$ data, without having to fit an equation of state or rely on model assumptions (see also Méndez et al., 2021, 2022), providing the first experimental constraints on the bulk modulus softening of ferropericlase at high temperature. In Fig. 1b, the experimentally determined bulk moduli are plotted as a function of pressure, together with our computational predictions and results from previous studies. Our experimental and theoretical results at 900-1000 K agree well overall; both show a broad and asymmetric spin crossover-induced softening of the bulk modulus between around 45 GPa and 105 GPa. Pressure cycling measurements performed at selected P-T conditions confirm the softening of the bulk modulus at seismic frequencies (SI fig. S14). There is good agreement between our results and Brillouin spectroscopy measurements at 900 K of the bulk modulus of $(Mg_{0.94}Fe_{0.06})O$ by Yang et al. (2016), although those measurements are limited to pressures below the spin crossover and made on a single-crystal sample of ferropericlase with lower iron content, in neon PTM. The ab initio calculations performed here also fit well with previous results from dDAC experiments at room temperature (Méndez et al., 2022).

In our new computations a random distribution of iron atoms in the crystal lattice is accounted for and rather than assuming ideal mixing of HS and LS states, the enthalpy of mixed spin states is calculated, in addition to full HS and LS states (see Méndez et al., 2022 for details). This is in contrast to older studies based on models assuming an ideal mixing of HS and LS iron and a uniform arrangement of iron atoms (Wentzcovitch et al., 2009; Wu et al., 2013). Comparison of our calculated bulk moduli with those of Wu et al. (2013) shows excellent agreement in regions where ferropericlase is in a pure high- or low-spin state, but differences emerge for the mixed-spin state (SI fig. S15). Similarly, differences in shear moduli are most pronounced in the mixed-spin region and

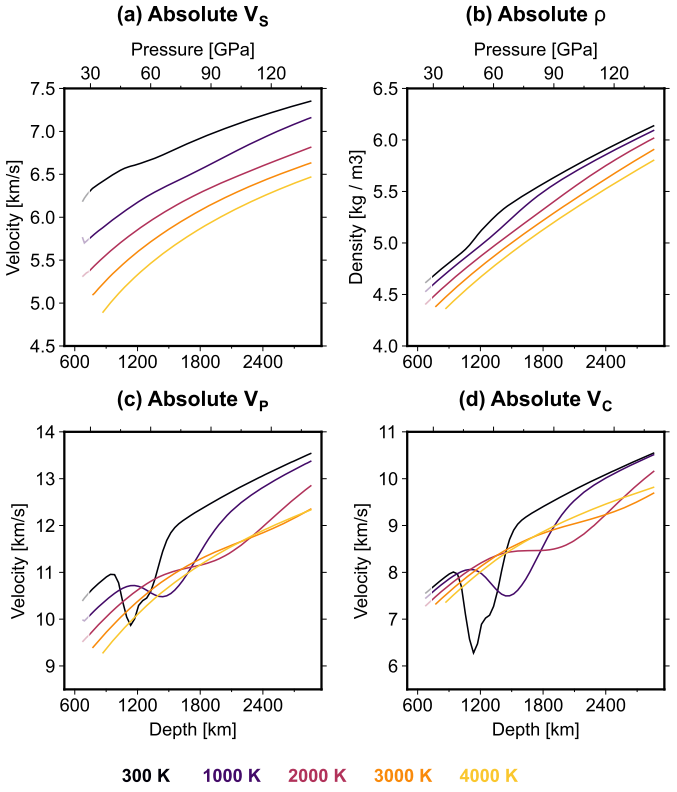

Fig. 2. Theoretical predictions of absolute (a) S-wave velocity V_S, (b) density ρ, (c) P-wave velocity V_P, and (d) bulk sound velocity V_C of ferropericlase as a function of depth in Earth's mantle. The iron spin crossover leads to a marked reduction in V_P and V_C, while V_S and ρ increase continuously with depth with only slight changes in slope.

increase at higher pressures and temperatures (SI fig. S16). This suggests that differences arise mainly from different values for the low-spin fraction of iron. Wu et al. (2013) predict a sharper bulk modulus softening over a narrower depth range and a larger amplitude than observed in our experimental results (Fig. 1b). More recent studies have taken into account a favourable enthalpy of mixing of HS and LS states (Holmström and Stixrude, 2015; Sun et al., 2022), but these predict a wider spin crossover than found in this work.

The agreement between our high-temperature experimental results and our computations at high temperature confirm the robustness of the later, allowing us to confidently extend the theoretical model to mantle temperatures. Our theoretical results for density (ρ) and seismic velocities (V_S, V_P and V_C) along several isotherms are shown in Fig. 2a-d for $(Mg_{0.8125}Fe_{0.1875})O$. Along a typical geotherm, the onset of the spin crossover is predicted to occur around 1500 km depth, while full low-spin state is never reached (SI fig. S17), indicating that spin crossover-induced changes to the physical properties of ferropericlase are expected to affect most of the lower mantle (see also Méndez et al., 2022). We find a substantial reduction in V_P and V_C across the spin crossover, while V_S and ρ are barely affected and increase continuously (Fig. 2a-d).

3.2. Signature of the spin crossover in seismic tomography

To understand how the signature of the spin crossover in ferropericlase will show up in data-based tomography models, we constructed synthetic seismic tomography models with and without the spin crossover, using the methodology described in section 2.3. Specifically, we combine the present-day temperature field of a high-resolution mantle circulation model (Davies et al., 2012; for details see Koelemeijer et al., 2018) with the temperature dependence of the spin crossover from our experimentally benchmarked calculations to create maps of the spin state and seismic velocity variations in the lower mantle (Fig. 3). The distribution of heterogeneity in the mantle circulation model is, to first order, consistent with the seismologically imaged distribution, as it is largely dictated by 300 Myr of prescribed surface plate velocities. The resulting ring of downwellings around the Pacific and upwelling return flow in the Pacific and under Africa cause temperature variations in the lower mantle (Fig. 3 top row). These temperature variations lead to substantial lateral variations in spin fractions at depths below 1800 km (Fig. 3 second row): low spin fractions are generally higher in cold regions with downgoing slabs than in hot regions with upwelling plumes.

In the bottom two rows of Fig. 3, bulk sound velocity variations are shown at different depths in the lower mantle for the HS (without the spin crossover) and MS (with the spin crossover) models. Our results clearly show that at depths where the elastic behaviour of ferropericlase is influenced by the spin crossover, bulk sound velocity variations are much less pronounced in the MS model compared to the HS model, indicating a lower sensitivity to temperature. In some regions, we even observe a positive correlation between temperature and bulk sound velocity, lower temperatures lead to negative velocity variations (e.g. at 1490 km depth) and higher temperatures lead to positive velocity variations (e.g. at 2122 km depth). This inversion of the temperature dependence can be explained by the shift of the bulk modulus softening in ferropericlase to higher pressures with increasing temperature, which leads to a positive temperature dependence of V_C $(= \sqrt{\frac{K}{\rho}})$ at specific P-T conditions (Fig. 1b and 2d), as previously suggested by Marquardt et al. (2009) and Wu (2016).

The seismic signature of the spin crossover becomes more evident when looking at the radially-averaged correlation between V_S and V_C variations in depth profiles of the synthetic tomographic models (Fig. 4a). The anti-correlated temperature dependence of shear and bulk sound velocity in the spin crossover depth range leads to a strong negative anomaly in the S-C correlation in the MS model with a maximum around 1800 km depth, which is absent in the HS model. A second minimum in the S-C correlation at lowermost mantle depths is the result of the bridgmanite to post-perovskite transition (Koelemeijer et al., 2018), which was included in the construction of the models.

To allow for a direct comparison between our high-resolution synthetic velocity models and data-derived seismic tomography models with a limited tomographic resolution, we apply a tomographic filter (see section 2.3). After filtering, the spin crossover signal in the depth profile of the mixed-spin synthetic tomography model becomes less pronounced, with a more smeared out and weakened negative S-C correlation (Fig. 4b). Nonetheless, differences between the HS and MS models remain clearly visible. The MS model shows a lower S-C correlation between 1200 km and 2300 km depth than the HS model, indicating that a negative anomaly in S-C correlation can serve as a distinguishing feature in seismic observations for the detection of the iron spin crossover, even if a realistic limited seismic resolution is accounted for.

A high V_S / V_P ratio has also been suggested in the past as a characteristic signature of the spin crossover (Marquardt et al., 2009). While we observe a modest increase in the ratio of V_S variations to V_P variations at mid-lower mantle depths in the high-resolution MS model as a result of the spin crossover (SI fig. S18), the differences between the HS and MS models largely disappear after tomographic filtering. This suggests that the S/P ratio is a less suitable measure for the detection of the spin crossover when accounting for the resolution achieved in current tomographic models.

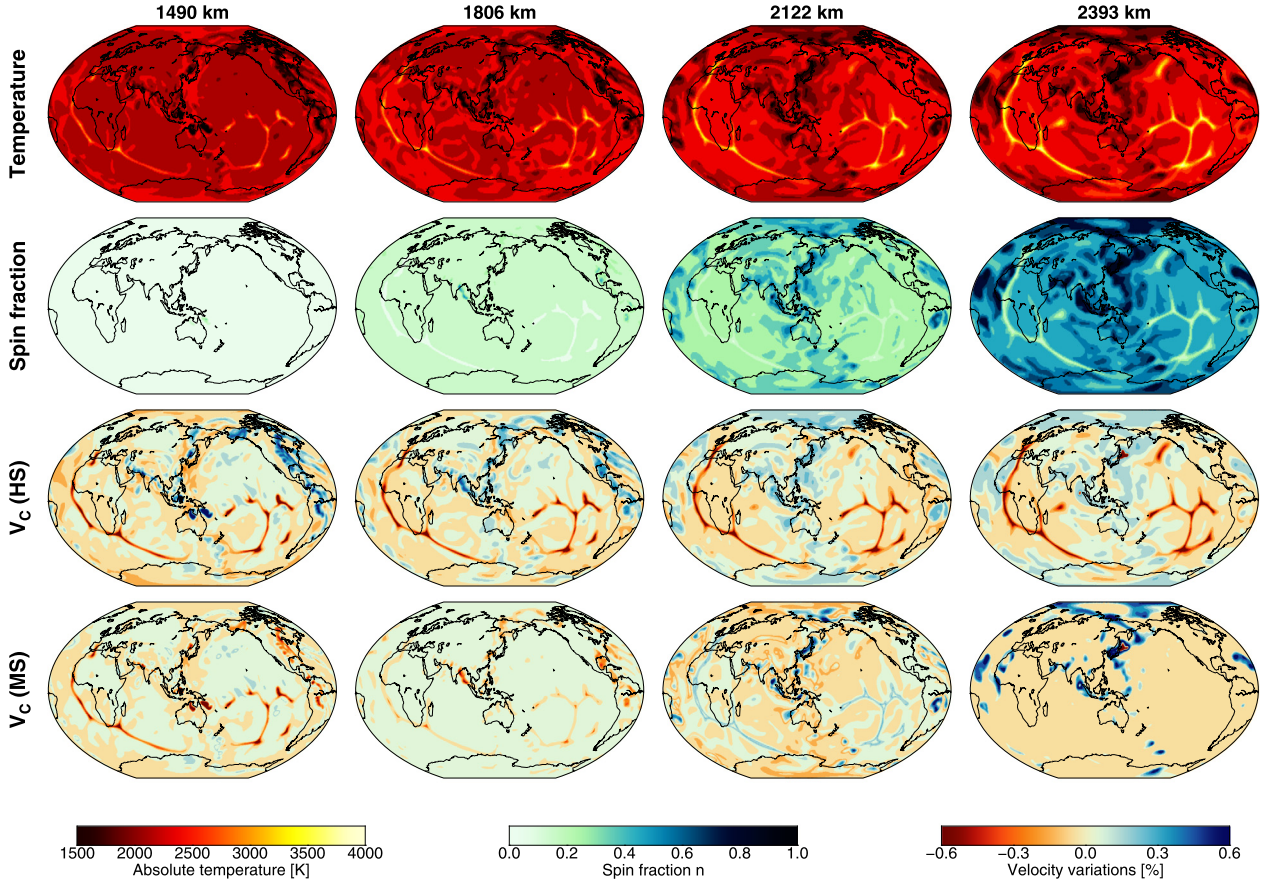

Fig. 3. Maps of temperature, spin fraction and bulk sound velocity variations for high-spin (HS) and mixed-spin (MS) ferropericlase at different depths in the lower mantle in our synthetic models. The top row shows the temperature field generated from a high-resolution geodynamic model and the second row shows the fraction of ferropericlase in the low-spin state corresponding to these temperatures, as predicted by ab- initio calculations. The last two rows show bulk sound velocity V_C variations in the high-resolution synthetic seismic tomography models when ferropericlase is assumed to stay in a high-spin state (HS model) and when the effects of spin fraction variations are included (MS model), respectively.

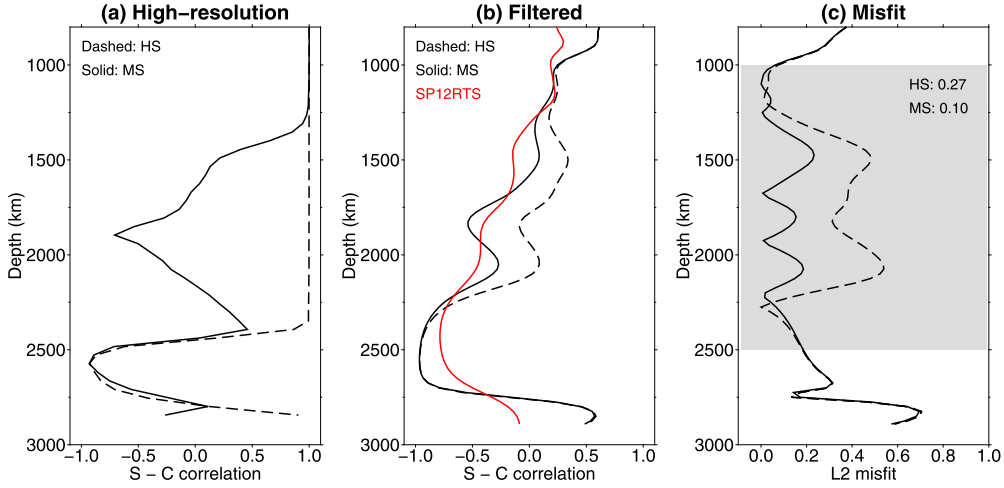

Fig. 4. Prediction of radially averaged correlation between V_S and V_C variations (S − C correlation) along depth profiles in the synthetic tomography models without the spin crossover (high-spin ferropericlase only, HS) and including the spin crossover (ferropericlase with P-T dependent mixed spin fractions MS), as dashed and solid lines, respectively. (a) Results without the application of a tomographic filter, showing a strong negative anomaly in the mid-lower mantle produced by the spin crossover. (b) Results of the synthetic models with tomographic filtering compared to seismic tomography model SP12RTS (red) (Koelemeijer et al., 2016). (c) L2 misfit between the predicted S - C correlations of the HS and MS models and model SP12RTS itself. The average misfit between 1000 and 2500 km depth (grey shaded region) is reduced by 63% from 0.27 (HS) to 0.1 (MS) when the effects of the iron spin crossover in ferropericlase are included.

When comparing our filtered synthetic tomography models to joint S- and P-wave model SP12RTS (Koelemeijer et al., 2016), we find that the negative S-C correlation at mid-lower mantle depths in SP12RTS is best reproduced by the synthetic model with ferropericlase in mixed-spin state (Fig. 4b). Inclusion of the spin crossover significantly affects the L2 misfit with model SP12RTS between 1000 and 2500 km depth, reducing it on average by 63%, from 0.27 (HS) to 0.10 (MS) (Fig. 4c). Since there is no other known

process that has the same effect on seismic velocities at these depths, our results strongly suggest that the negative S-C correlation in the mid-lower mantle is caused by the iron spin crossover in ferropericlase. Our work thus provides the first evidence for the visibility of the iron spin crossover in ferropericlase in seismic tomography models while taking realistic tomographic resolution into account. This finding implies the presence of about 20% of ferropericlase throughout the lower mantle, supporting recent works in favour of a pyrolitic lower mantle composition (Kurnosov et al., 2017; Wang et al., 2015; Zhang et al., 2016), as opposed to a perovskitic average composition (Murakami et al., 2012).

If the depth resolution in seismic tomography models describing V_C variations improves in the future, a more detailed mapping of the spin crossover might become feasible and could ultimately allow for pinpointing average mantle temperature at mid-lower mantle depths, as well as lateral temperature variations from comparisons between synthetic and data-derived tomographic models. In areas of the mantle were subducting slabs cause cold downwellings, the spin crossover-induced changes in ferropericlase properties will occur at shallower depths as compared to the radial average, and the magnitude of the Vc softening will be larger (Fig. 2d). This would make the seismic signature of the spin crossover easier to detect, consistent with the observations of Shephard et al. (2021). In contrast, in hot areas of the mantle (e.g. superplumes), the maximum Vc softening would be weaker and shifted to greater depths, near the core-mantle boundary (see also Méndez et al. (2022)).

Our theoretical computations, that are used for the construction of the seismic tomography models are for a single composition of ferropericlase, i.e. an iron content of 18.75 at.%. Although this is close to the composition expected for the majority of the lower mantle (Irifune et al., 2010; Murakami, 2005), it has been suggested that the iron partitioning between ferropericlase and bridgmanite is affected by the spin crossover, leading to an increase of iron content of ferropericlase (Lin et al., 2013). In addition, ferropericlase may be enriched in iron in the lowermost mantle and the low seismic velocities in Ultra Low-Velocity Zones (ULVZs) have been attributed to the presence of iron-rich ferropericlase (Wicks et al., 2010, 2017). The spin crossover-induced bulk modulus softening is expected to shift to higher pressures with increasing iron content (Solomatova et al., 2016), so compositional variations in lower mantle-ferropericlase would affect the spin state, in addition to temperature variations. Such mechanisms should be considered in future studies to further resolve the spin state of the lower mantle and its effect on mantle physical properties.

Other mantle minerals, most importantly bridgmanite, may also undergo a spin crossover at mantle pressures (e.g. Badro et al., 2004; Badro, 2014; Lin et al., 2013). However, despite ongoing research, any possible effects of a spin crossover in bridgmanite on elastic properties are not yet well-constrained (e.g. Fu et al., 2018; Okuda et al., 2020; Zhu et al., 2020) and likely weaker, and were therefore not included in the construction of our seismic velocity models. The methodology used in the present work may be adopted in future studies to resolve the effects of iron content of ferropericlase and a spin crossover in bridgmanite on global seismic tomography.

4. Conclusions

First experimental results on the spin crossover-induced elastic softening in ferropericlase at high temperature are reproduced by a new theoretical model that takes the position of iron atoms in the crystal lattice into account. By combining the experimentally-verified computations with the present-day temperature distribution in the mantle predicted by geodynamics, we constructed high-resolution synthetic seismic tomography models. The theoretically expected seismic signature of the spin crossover in the lower mantle is expressed as a strong negative anomaly in the S-C correlation and a moderately increased S/P ratio. After applying a tomographic filter to account for a realistic tomographic resolution of data-driven tomography models, we find that a negative S-C correlation is the most suitable measure for detection of the spin crossover in seismic observations. Including the spin crossover in the filtered synthetic model improves the fit in the S-C correlation with global tomography model SP12RTS between 1000 and 2500 km depth by 63%. Our findings provide the first evidence for the visibility of the spin crossover in seismic tomography models when realistic tomographic resolution is accounted for and hence indicate the presence of mixed-spin ferropericlase in large parts of the lower mantle. Improvement of seismic resolution will facilitate a detailed mapping of the spin crossover using the S-C correlation. In the future, this may be translated to 3D maps of temperature and iron distribution in the mid-lower mantle, by reversing the protocol employed in this study.

CRediT authorship contribution statement

Viktoria E. Trautner: Writing – review & editing, Writing – original draft, Visualization, Formal analysis. **Stephen Stackhouse:** Writing – review & editing, Writing – original draft, Visualization, Methodology, Funding acquisition, Conceptualization. **Alice R. Turner:** Writing – review & editing, Formal analysis. **Paula Koelemeijer:** Writing – review & editing, Writing – original draft, Visualization, Supervision, Methodology, Funding acquisition, Conceptualization. **D. Rhodri Davies:** Writing – review & editing, Methodology. **Alba San José Méndez:** Writing – review & editing, Investigation. **Niccolo Satta:** Writing – review & editing, Investigation. **Alexander Kurnosov:** Investigation. **Hanns-Peter Liermann:** Writing – review & editing, Methodology. **Hauke Marquardt:** Writing – review & editing, Writing – original draft, Supervision, Project administration, Funding acquisition, Conceptualization.

Declaration of competing interest

The authors declare that they have no known competing financial interests or personal relationships that could have appeared to influence the work reported in this paper.

Data availability

Data is available as separate tables in the Supplementary material.

Acknowledgements

This research received funding through the European Union's Horizon 2020 research and innovation Programme (ERC grant DEEP-MAPS, ID: 864877 awarded to HM), as well as from NERC (grant number NE/K006290/1 awarded to SS) and from Royal Society grants awarded to PK (RGF\EA\181029 and URF\R1\180377). The authors acknowledge DESY (Hamburg, Germany), a member of the Helmholtz Association HGF, for the provision of experimental facilities. The calculations were performed on ARC3 and ARC4, part of the High-Performance Computing facilities at the University of Leeds, United Kingdom. PK would like to thank Carolina Lithgow-Bertelloni and Lars Stixrude for providing the thermodynamic database used for converting the temperature distribution to seismic velocities. We thank two anonymous reviewers for constructive comments, which helped improve the manuscript.

Appendix A. Supplementary material

Supplementary material related to this article can be found online at https://doi.org/10.1016/j.epsl.2023.118296.

References

Badro, J., Fiquet, G., Guyot, F., Rueff, J.-P., Struzhkin, V.V., Vankó, G., Monaco, G., 2003. Iron partitioning in Earth's mantle: toward a deep lower mantle discontinuity. Science 300 (5620), 789–791. https://doi.org/10.1126/science.1081311.

Badro, J., Rueff, J.-P., Vankó, G., Monaco, G., Fiquet, G., Guyot, F., 2004. Electronic transitions in perovskite: possible nonconvecting layers in the lower mantle. Science 305 (5682), 383–386. https://doi.org/10.1126/science.1098840.

Badro, J., 2014. Spin transitions in mantle minerals. Annu. Rev. Earth Planet. Sci. 42 (1), 231–248. https://doi.org/10.1146/annurev-earth-042711-105304.

Birch, F., 1947. Finite elastic strain of cubic crystals. Phys. Rev. 71 (11), 809–824. https://doi.org/10.1103/PhysRev.71.809.

Blöchl, P.E., 1994. Projector augmented-wave method. Phys. Rev. B 50 (24), 17953–17979. https://doi.org/10.1103/PhysRevB.50.17953.

Cammarano, F., Marquardt, H., Speziale, S., Tackley, P.J., 2010. Role of iron-spin transition in ferropericlase on seismic interpretation: a broad thermochemical transition in the mid mantle? Geophys. Res. Lett. 37 (3), L03308. https://doi.org/10.1029/2009gl041583.

Crowhurst, J.C., Brown, J.M., Goncharov, A.F., Jacobsen, S.D., 2008. Elasticity of (Mg, Fe)O through the spin transition of iron in the lower mantle. Science 319 (5862), 451–453. https://doi.org/10.1126/science.1149606.

Davies, D.R., Goes, S., Davies, J.H., Schuberth, B.S.A., Bunge, H.P., Ritsema, J., 2012. Reconciling dynamic and seismic models of Earth's lower mantle: the dominant role of thermal heterogeneity. Earth Planet. Sci. Lett. 353-354, 253–269. https://doi.org/10.1016/j.epsl.2012.08.016.

Dong, W., Glazyrin, K., Khandarkhaeva, S., Fedotenko, T., Bednarčík, J., Greenberg, E., et al., 2022. Fe0.79Si0.07B0.14 metallic glass gaskets for high-pressure research beyond 1 Mbar. J. Synchrotron Radiat. 29 (5), 1167–1179. https://doi.org/10.1107/s1600577522007573.

Dudarev, S.L., Botton, G.A., Savrasov, S.Y., Humphreys, C.J., Sutton, A.P., 1998. Electron-energy-loss spectra and the structural stability of nickel oxide: an LSDA+U study. Phys. Rev. B 57 (3), 1505–1509. https://doi.org/10.1103/PhysRevB.57.1505.

Fei, Y., Ricolleau, A., Frank, M., Mibe, K., Shen, G., Prakapenka, V., 2007a. Toward an internally consistent pressure scale. Proc. Natl. Acad. Sci. USA 104 (22), 9182–9186. https://doi.org/10.1073/pnas.0609013104.

Fei, Y., Zhang, L., Corgne, A., Watson, H., Ricolleau, A., Meng, Y., Prakapenka, V., 2007b. Spin transition and equations of state of (Mg, Fe)O solid solutions. Geophys. Res. Lett. 34 (17), L17307. https://doi.org/10.1029/2007gl030712.

Fu, S., Yang, J., Zhang, Y., Okuchi, T., Mccammon, C., Kim, H.I., et al., 2018. Abnormal elasticity of Fe-bearing bridgmanite in the Earth's lower mantle. Geophys. Res. Lett. 45 (10), 4725–4732. https://doi.org/10.1029/2018gl077764.

Holmström, E., Stixrude, L., 2015. Spin crossover in ferropericlase from first-principles molecular dynamics. Phys. Rev. Lett. 114 (11), 117202. https://doi.org/10.1103/PhysRevLett.114.117202.

Irifune, T., Shinmei, T., McCammon, C.A., Miyajima, N., Rubie, D.C., Frost, D.J., 2010. Iron partitioning and density changes of pyrolite in Earth's lower mantle. Science 327 (5962), 193–195. https://doi.org/10.1126/science.1181443.

Kennett, B.L.N., 2021. The relative behaviour of bulk and shear modulus as an indicator of the iron spin transition in the lower mantle. Earth Planet. Sci. Lett. 559. https://doi.org/10.1016/j.epsl.2021.116808.

Koelemeijer, P., Ritsema, J., Deuss, A., Van Heijst, H.-J., 2016. SP12RTS: a degree-12 model of shear- and compressional-wave velocity for Earth's mantle. Geophys. J. Int. 204 (2), 1024–1039. https://doi.org/10.1093/gji/ggv481.

Koelemeijer, P., Schuberth, B.S.A., Davies, D.R., Deuss, A., Ritsema, J., 2018. Constraints on the presence of post-perovskite in Earth's lowermost mantle from tomographic-geodynamic model comparisons. Earth Planet. Sci. Lett. 494, 226–238. https://doi.org/10.1016/j.epsl.2018.04.056.

Komabayashi, T., Hirose, K., Nagaya, Y., Sugimura, E., Ohishi, Y., 2010. High-temperature compression of ferropericlase and the effect of temperature on iron spin transition. Earth Planet. Sci. Lett. 297 (3–4), 691–699. https://doi.org/10.1016/j.epsl.2010.07.025.

Kresse, G., Furthmüller, J., 1996a. Efficient iterative schemes for ab initio total-energy calculations using a plane-wave basis set. Phys. Rev. B 54 (16), 11169–11186. https://doi.org/10.1103/PhysRevB.54.11169.

Kresse, G., Furthmüller, J., 1996b. Efficiency of ab-initio total energy calculations for metals and semiconductors using a plane-wave basis set. Comput. Mater. Sci. 6 (1), 15–50. https://doi.org/10.1016/0927-0256(96)00008-0.

Kresse, G., Joubert, D., 1999. From ultrasoft pseudopotentials to the projector augmented-wave method. Phys. Rev. B 59 (3), 1758–1775. https://doi.org/10.1103/PhysRevB.59.1758.

Kurnosov, A., Marquardt, H., Frost, D.J., Ballaran, T.B., Ziberna, L., 2017. Evidence for a Fe3+-rich pyrolitic lower mantle from (Al, Fe)-bearing bridgmanite elasticity data. Nature 543 (7646), 543–546. https://doi.org/10.1038/nature21390.

Lin, J.-F., Struzhkin, V.V., Jacobsen, S.D., Hu, M.Y., Chow, P., Kung, J., et al., 2005. Spin transition of iron in magnesiowüstite in the Earth's lower mantle. Nature 436 (7049), 377–380. https://doi.org/10.1038/nature03825.

Lin, J.-F., Speziale, S., Mao, Z., Marquardt, H., 2013. Effects of the electronic spin transitions of iron in lower mantle minerals: implications for deep mantle geophysics and geochemistry. Rev. Geophys. 51 (2), 244–275. https://doi.org/10.1002/rog.20010.

Mao, Z., Lin, J.-F., Liu, J., Prakapenka, V.B., 2011. Thermal equation of state of lower-mantle ferropericlase across the spin crossover. Geophys. Res. Lett. 38 (23), L23308. https://doi.org/10.1029/2011gl049915.

Marquardt, H., Speziale, S., Reichmann, H.J., Frost, D.J., Schilling, F.R., 2009. Single-crystal elasticity of (Mg0.9Fe0.1)O to 81 GPa. Earth Planet. Sci. Lett. 287 (3–4), 345–352. https://doi.org/10.1016/j.epsl.2009.08.017.

Marquardt, H., Miyagi, L., 2015. Slab stagnation in the shallow lower mantle linked to an increase in mantle viscosity. Nat. Geosci. 8 (4), 311–314. https://doi.org/10.1038/ngeo2393.

Marquardt, H., Buchen, J., Mendez, A.S.J., Kurnosov, A., Wendt, M., Rothkirch, A., et al., 2018. Elastic softening of (Mg0.8Fe0.2)O ferropericlase across the iron spin crossover measured at seismic frequencies. Geophys. Res. Lett. 45 (14), 6862–6868. https://doi.org/10.1029/2018gl077982.

Méndez, A.S.J., Marquardt, H., Husband, R.J., Schwark, I., Mainberger, J., Glazyrin, K., et al., 2020. A resistively-heated dynamic diamond anvil cell (RHdDAC) for fast compression x-ray diffraction experiments at high temperatures. Rev. Sci. Instrum. 91 (7), 073906. https://doi.org/10.1063/5.0007557.

Méndez, A.S.J., Trybel, F., Husband, R.J., Steinle-Neumann, G., Liermann, H.-P., Marquardt, H., 2021. Bulk modulus of H2O across the ice VII–ice X transition measured by time-resolved x-ray diffraction in dynamic diamond anvil cell experiments. Phys. Rev. B 103 (6), 064104. https://doi.org/10.1103/physrevb.103.064104.

Méndez, A.S.J., Stackhouse, S., Trautner, V., Wang, B., Satta, N., Kurnosov, A., et al., 2022. Broad elastic softening of (Mg, Fe)O ferropericlase across the iron spin crossover and a mixed-spin lower mantle. J. Geophys. Res., Solid Earth 127 (8), e2021JB023832. https://doi.org/10.1029/2021jb023832.

Muir, J.M.R., Brodholt, J.P., 2015. Elastic properties of ferropericlase at lower mantle conditions and its relevance to ULVZs. Earth Planet. Sci. Lett. 417, 40–48. https://doi.org/10.1016/j.epsl.2015.02.023.

Murakami, M., 2005. Post-perovskite phase transition and mineral chemistry in the pyrolitic lowermost mantle. Geophys. Res. Lett. 32 (3). https://doi.org/10.1029/2004gl021956.

Murakami, M., Ohishi, Y., Hirao, N., Hirose, K., 2012. A perovskitic lower mantle inferred from high-pressure, high-temperature sound velocity data. Nature 485 (7396), 90–94. https://doi.org/10.1038/nature11004.

Murnaghan, F.D., 1944. The compressibility of media under extreme pressures. Proc. Natl. Acad. Sci. 30 (9), 244–247. https://doi.org/10.1073/pnas.30.9.244.

Nosé, S., 1984. A unified formulation of the constant temperature molecular dynamics methods. J. Chem. Phys. 81 (1), 511–519. https://doi.org/10.1063/1.447334.

Oganov, A.R., Brodholt, J.P., Price, G.D., 2001. Ab initio elasticity and thermal equation of state of MgSiO3 perovskite. Earth Planet. Sci. Lett. 184 (3), 555–560. https://doi.org/10.1016/S0012-821X(00)00363-0.

Okuda, Y., Ohta, K., Sinmyo, R., Hirose, K., Ohishi, Y., 2020. Anomalous compressibility in (Fe, Al)-bearing bridgmanite: implications for the spin state of iron. Phys. Chem. Miner. 47 (9). https://doi.org/10.1007/s00269-020-01109-3.

Pennicard, D., Smoljanin, S., Pithan, F., Sarajlic, M., Rothkirch, A., Yu, Y., et al., 2018. LAMBDA 2M GaAs—a multi-megapixel hard X-ray detector for synchrotrons. J. Instrum. 13 (1), C01026. https://doi.org/10.1088/1748-0221/13/01/C01026.

Perdew, J.P., Zunger, A., 1981. Self-interaction correction to density-functional approximations for many-electron systems. Phys. Rev. B 23 (10), 5048.

Prescher, C., Prakapenka, V.B., 2015. DIOPTAS: a program for reduction of two-dimensional X-ray diffraction data and data exploration. High Press. Res. 35 (3), 223–230. https://doi.org/10.1080/08957959.2015.1059835.

Shephard, G.E., Houser, C., Hernlund, J.W., Valencia-Cardona, J.J., Trønnes, R.G., Wentzcovitch, R.M., 2021. Seismological expression of the iron spin crossover in ferropericlase in the Earth's lower mantle. Nat. Commun. 12 (1). https://doi.org/10.1038/s41467-021-26115-z.

Singh, A.K., Takemura, K., 2001. Measurement and analysis of nonhydrostatic lattice strain component in niobium to 145 GPa under various fluid pressure-transmitting media. J. Appl. Phys. 90 (7), 3269–3275. https://doi.org/10.1063/1.1397283.

Sinmyo, R., Hirose, K., 2010. The Soret diffusion in laser-heated diamond-anvil cell. Phys. Earth Planet. Inter. 180 (3–4), 172–178. https://doi.org/10.1016/j.pepi.2009.10.011.

Solomatova, N.V., Jackson, J.M., Sturhahn, W., Wicks, J.K., Zhao, J., Toellner, T.S., et al., 2016. Equation of state and spin crossover of (Mg, Fe)O at high pressure, with implications for explaining topographic relief at the core-mantle boundary. Am. Mineral. 101 (5), 1084–1093. https://doi.org/10.2138/am-2016-5510.

Stixrude, L., Lithgow-Bertelloni, C., 2011. Thermodynamics of mantle minerals - II. Phase equilibria. Geophys. J. Int. 184 (3), 1180–1213. https://doi.org/10.1111/j.1365-246x.2010.04890.x.

Stixrude, L., Lithgow-Bertelloni, C., 2022. Thermal expansivity, heat capacity and bulk modulus of the mantle. Geophys. J. Int. 228 (2), 1119–1149.

Sun, Y., Zhuang, J., Wentzcovitch, R.M., 2022. Thermodynamics of spin crossover in ferropericlase: an improved LDA+Usc calculation. Electron. Struct. 4, 014008. https://doi.org/10.1088/2516-1075/ac522b.

Tsuchiya, T., Wentzcovitch, R.M., Da Silva, C.R.S., De Gironcoli, S., 2006. Spin transition in magnesiowüstite in Earth's lower mantle. Phys. Rev. Lett. 96 (19). https://doi.org/10.1103/physrevlett.96.198501.

Wang, B., 2022. Batch Peaks Fitting Script in Python for Time-Resolved XRD Data Analysis (v1.0.0). Software, Zenodo.

Wang, X., Tsuchiya, T., Hase, A., 2015. Computational support for a pyrolitic lower mantle containing ferric iron. Nat. Geosci. 8 (7), 556–559. https://doi.org/10.1038/ngeo2458.

Waychunas, G.A., Dollase, W.A., Ross II, C.R., 1994. Short-range order measurements in MgO-FeO and MgO-LiFeO, solid solutions by DLS simulation-assisted EXAFS analysis. Am. Mineral. 79 (3–4), 274–288.

Wentzcovitch, R.M., Justo, J.F., Wu, Z., Da Silva, C.R.S., Yuen, D.A., Kohlstedt, D., 2009. Anomalous compressibility of ferropericlase throughout the iron spin crossover. Proc. Natl. Acad. Sci. 106 (21), 8447–8452. https://doi.org/10.1073/pnas.0812150106.

Wicks, J.K., Jackson, J.M., Sturhahn, W., 2010. Very low sound velocities in iron-rich (Mg, Fe)O: implications for the core-mantle boundary region. Geophys. Res. Lett. 37 (15), L15304. https://doi.org/10.1029/2010gl043689.

Wicks, J.K., Jackson, J.M., Sturhahn, W., Zhang, D., 2017. Sound velocity and density of magnesiowüstites: implications for ultralow-velocity zone topography. Geophys. Res. Lett. 44 (5), 2148–2158. https://doi.org/10.1002/2016gl071225.

Wu, Z., Justo, J.F., Wentzcovitch, R.M., 2013. Elastic anomalies in a spin-crossover system: ferropericlase at lower mantle conditions. Phys. Rev. Lett. 110 (22), 228501. https://doi.org/10.1103/PhysRevLett.110.228501.

Wu, Z., 2016. Velocity structure and composition of the lower mantle with spin crossover in ferropericlase. J. Geophys. Res., Solid Earth 121 (4), 2304–2314. https://doi.org/10.1002/2015jb012667.

Yang, J., Tong, X., Lin, J.-F., Okuchi, T., Tomioka, N., 2015. Elasticity of ferropericlase across the spin crossover in the Earth's lower mantle. Sci. Rep. 5 (1), 17188. https://doi.org/10.1038/srep17188.

Yang, J., Lin, J.F., Jacobsen, S.D., Seymour, N.M., Tkachev, S.N., Prakapenka, V.B., 2016. Elasticity of ferropericlase and seismic heterogeneity in the Earth's lower mantle. J. Geophys. Res., Solid Earth 121 (12), 8488–8500. https://doi.org/10.1002/2016jb013352.

Zhang, S., Cottaar, S., Liu, T., Stackhouse, S., Militzer, B., 2016. High-pressure, temperature elasticity of Fe- and Al-bearing MgSiO3: Implications for the Earth's lower mantle. Earth Planet. Sci. Lett. 434 (C), 264–273. https://doi.org/10.1016/j.epsl.2015.11.030.

Zhu, F., Liu, J., Lai, X., Xiao, Y., Prakapenka, V., Bi, W., et al., 2020. Synthesis, elasticity, and spin state of an intermediate MgSiO3-FeAlO3 bridgmanite: implications for iron in Earth's lower mantle. J. Geophys. Res., Solid Earth 125 (7). https://doi.org/10.1029/2020jb019964.